Journal of
Mechanics of
Materials and Structures

FRACTURE MECHANICS ANALYSIS OF THREE-DIMENSIONAL ION CUT TECHNOLOGY

Xi-Qiao Feng, Mei Xu, Xuyue Wang and Bin Gu

Volume 2, Nº 9 November 2007

mathematical sciences publishers

JOURNAL OF MECHANICS OF MATERIALS AND STRUCTURES
Vol. 2, No. 9, 2007

FRACTURE MECHANICS ANALYSIS OF THREE-DIMENSIONAL ION CUT TECHNOLOGY

XI-QIAO FENG, MEI XU, XUYUE WANG AND BIN GU

The recently established ion cut technology enables accurate fabrication of silicon-on-insulator (SOI) wafers and has found some other significant applications. We study fracture mechanics of the technology when directly cutting a wafer into a desired surface morphology. First, we describe integral transform-based methods for calculating the stress intensity factors of subsurface cracks embedded in a semiinfinite solid. Because the crack and the free surface interact, the crack tip fields are generally of I-II mixed mode. We derive solutions for plane-strain or axisymmetrical configurations. We then analyze the suggested three-dimensional ion cut method using the fracture criterion for kinking propagation of a mixed-mode crack. To illustrate the approach, we consider circular hole and straight groove surface patterns.

1. Introduction

Silicon-on-insulator (SOI) wafers have been used extensively as the starting materials for ultralarge-scale integration (ULSI) device structures. A typical SOI system consists of a thin layer of single-crystal silicon supported by an underlying insulator (for example, SiO_2 and sapphire). SOI wafer structures have important advantages over bulk or epitaxial starting wafers for a wide range of ULSI applications [Colinge 1991; Haisma and Spierings 2002]. SOI wafers potentially offer fast circuit performance and packing density, immunity from latch-up, low power consumption, high resistance to ionizing radiation, and simplified processing compared to bulk or epitaxial silicon. Hence, they appear ideal for making leading edge integrated circuits with high speed and transistor count but also low voltage and power operation, leading to better performance in battery operated systems, such as portable logic or microprocessor ICs. Two conventional and commercially-available methods for making SOI wavers are the separation-by-implanted oxygen (SIMOX) method and the bonded silicon-on-insulator (BSOI) method [Colinge 1991]. However, neither is suited to industrial-scale production.

In 1995, Bruel [1995; 1996], Aspar et al. [1996], and Aspar et al. [1999] at LETI developed a novel technique, Smart-Cut™, a registered trademark of SOITEC, for fabricating high-quality SOI systems. This process skillfully combines hydrogen implantation and wafer bonding, and involves four main steps: (1) Through hydrogen ion implantation, a wafer A capped with a dielectric layer (for example, SiO_2) is imparted a thin layer of sufficiently dense hydrogen ions. (2) The wafer A is then bonded with a handle wafer B. (3) The bonded wafer is then split and annealed through two stages of heating, first at medium-temperature (400–600° C), and then at high-temperature (about 1100° C). In the first heating

Keywords: crack, fracture, stress intensity factor, integral transform method, ion cut technology.
The authors gratefully acknowledge support from the National Natural Science Foundation of China (Grant Nos. 10525210 and 10121202), the 973 Project (Grant No. 2004CB619303) and the GE-Tsinghua Propulsion Center. Bin Gu wishes to thank the Australian Research Council (ARC) for financial support.

stage, numerous microcracks appear at the depth of the maximum hydrogen ion concentration. The wafer A then splits into two parts, yielding an SOI structure and the remainder of wafer A. (4) The SOI layer is polished using a chemical-mechanical method to produce a high-quality surface.

The basic principle behind the Smart-Cut technology applies for fabricating single-crystal silicon or semiconductor films transferred onto different types of substrates (for example, glass and metals) [Bruel 1995; Bruel 1996; Aspar et al. 1996; Aspar et al. 1999; Tong and Bower 1998]. This technique has several significant advantages over traditional SOI synthesis methods such as SIMOX and BSOI. First, the Smart-Cut process helps ensure the wafers are accurate in thickness to less than 4 nm, compared to (20–30 nm) for conventional methods. Second, the SOI systems have high crystalline quality from using medium implantation doses of the smallest ion (H^+) and the final fine polishing. Third, ULSI devices based on the Smart-Cut wafers exhibit electrical characteristics comparable to or better than those made on bulk silicon wafers. Fourth, the Smart-Cut process can be performed using the standard equipment of microelectronics facilities, an important consideration for large-scale industrial production.

Since it was first published by Bruel [1995], the Smart-Cut technology has attracted considerable attention and found various applications. Using the technique, Tong and Bower [1998] transformed Si, Ge, and SiC films on substrates of a high melting temperature glass. Aspar et al. [1999] and Jalaguier et al. [1998] obtained some new structures with thin films of Si, GaAs or InP on silicon substrates by combining the Smart-Cut process with metal bonding. Di Cioccio et al. [1997] used the Smart-Cut technology to make *silicon carbide-on-insulator* structures. By implanting erbium into the top layer of a Smart-Cut SOI wafer, Gad et al. [2003] fabricated single-mode SOI waveguides with good optical quality. Recently, Feng and Huang [2004] studied the fundamental physics and mechanics of the Smart-Cut technology.

The previous Smart-Cut process synthesizes smooth SOI wafers that are highly uniform in thickness. Some wafer patterns, such as grooves and holes, still need to be prepared using more complicated manufacturing procedures. In this paper, we suggest extending the Smart-Cut technique to produce three-dimensional patterns. Hydrogen ions are not implanted into the whole wafer, but instead directed to localized regions by a specialized metal mask. In the heating stages, microcracks will still form to remove the unwanted material, leaving the designed surface pattern.

In the present paper, we analyze theoretically the three-dimensional ion cut method using linear elastic fracture mechanics. In Section 2, we present integral transform methods for finding the stress intensity factors (SIFs) for subsurface cracks in a semiinfinite space. We discuss two typical classes of crack configurations, plane strain and axisymmetrical problems. In Section 3, we apply the above integral transform methods to generate the feasibility conditions for pattern cutting by hydrogen ion implantation.

2. Integral transform methods for subsurface cracks

Engineers are generally interested in near-surface or subsurface cracks because they appear in a variety of engineered structures [Spence and Sharp 1985; Hutchinson and Suo 1992]. Subsurface cracks may form for various reasons, for example, thermal or residual stresses due to welding or other processes, contact fatigue stresses, preexisting defects beneath subsurfaces, or relatively weak interfaces in layered or laminated structures. Srivastava and Singh [1969] analyzed the effect of a penny-shaped crack on the stress field in a semiinfinite solid. Other researchers have studied the fracture mechanisms of subsurface cracks under different loading conditions, for example, contact, wear, and indentation [Komvopoulos

1996; Ma and Hwang 1996; Goshima and Soda 1997; Dyskin et al. 2000; Zhang et al. 2002; 2005; Feng and Xu 2006]. Fleming and Suh [1977] studied how surface traction helped propagate a horizontal subsurface crack. Cao [2002] presented a finite element model to determine subsurface median cracking in a trilayer sandwich subjected to contact loading. Bunger and Detournay [2005] and Zhang et al. [2002; 2005] studied the asymptotic behaviors of penny-shaped hydraulic cracks. Dyskin et al. [2000] employed the beam and dipole asymptotic approaches to analyze the interaction of a crack with parallel free boundaries. Despite the extensive interest, however, the community has not produced efficient methods for deriving the SIFs of subsurface cracks due to the crack-free surface interaction [Ma et al. 2005]. Therefore, with the aim of extending the ion cut method to surface pattern formation, we present in this section a method for calculating the SIFs of subsurface cracks using singular integral equation methods based on integral transforms. For illustration, we consider several typical subsurface crack configurations, although the presented methods may work for other configurations as well.

2.1. ***Axisymmetrical problems.*** Consider a circular crack beneath and parallel to the free surface of a semiinfinite body and subjected to an internal pressure p, as shown in Figure 1. Denote the crack radius as c, and its distance from the free surface as h. Refer to a cylindrical coordinate system (r, θ, z). For axisymmetrical problems, the stress equilibrium equations read

$$\frac{\partial \sigma_{rr}}{\partial r} + \frac{\partial \sigma_{rz}}{\partial z} + \frac{\sigma_{rr} - \sigma_{\theta\theta}}{r} = 0, \qquad \frac{\partial \sigma_{rz}}{\partial r} + \frac{\partial \sigma_{zz}}{\partial z} + \frac{\sigma_{rz}}{r} = 0, \tag{2–1}$$

and the strain-displacement relations are

$$\varepsilon_{rr} = \frac{\partial u}{\partial r}, \qquad \varepsilon_{\theta\theta} = \frac{u}{r}, \qquad \varepsilon_{rz} = \frac{1}{2}\left(\frac{\partial u}{\partial z} + \frac{\partial w}{\partial r}\right), \qquad \varepsilon_{zz} = \frac{\partial w}{\partial z}, \tag{2–2}$$

where σ_{ij} denote the stresses, ε_{ij} denote the strains, $u = u_r$ and $w = u_z$ are the nonzero displacements. Since the constitutive relation of single crystalline silicon is of weak anisotropy, the material is assumed throughout the paper to be linearly elastic and isotropic, with Young's modulus E and Poisson's ratio ν. Using Equation (2–2) and Hooke's law, the equilibrium equations in Equation (2–1) can be reexpressed

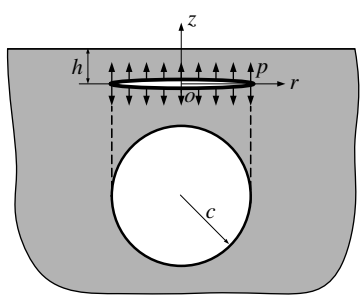

Figure 1. A circular subsurface crack beneath the free surface of a semiinfinite body.

in terms of the displacement components u and w as

$$\begin{aligned}(\kappa+1)\left(\frac{\partial^2 u}{\partial r^2}+\frac{1}{r}\frac{\partial u}{\partial r}-\frac{u}{r^2}+\frac{\partial^2 w}{\partial r\partial z}\right)+(\kappa-1)\left(\frac{\partial^2 u}{\partial z^2}-\frac{\partial^2 w}{\partial r\partial z}\right)=0,\\ (\kappa+1)\left(\frac{\partial^2 u}{\partial r\partial z}+\frac{1}{r}\frac{\partial u}{\partial z}+\frac{\partial^2 w}{\partial z^2}\right)-(\kappa-1)\left(\frac{\partial^2 u}{\partial r\partial z}-\frac{\partial^2 w}{\partial r^2}\right)-\frac{\kappa-1}{r}\left(\frac{\partial u}{\partial z}-\frac{\partial w}{\partial r}\right)=0,\end{aligned} \tag{2–3}$$

where $\kappa = 3-4\nu$.

To solve Equation (2–3), introduce in the radial variable the Hankel transforms $\tilde{u}$ and $\tilde{w}$ of the displacements u and w by

$$u(r,z)=\int_0^\infty \tilde{u}(z,\rho)\rho J_1(r\rho)d\rho, \qquad w(r,z)=\int_0^\infty \tilde{w}(z,\rho)\rho J_0(r\rho)d\rho, \tag{2–4}$$

where J_0 and J_1 are Bessel functions.

Substituting Equation (2–4) into the partial differential equations in Equation (2–3) yields the ordinary differential equations

$$\begin{aligned}(\kappa+1)\tilde{u}\rho^2-2\frac{\partial\tilde{w}}{\partial z}\rho+(\kappa-1)\frac{\partial^2\tilde{u}}{\partial z^2}=0,\\ (\kappa-1)\tilde{w}\rho^2-2\frac{\partial\tilde{u}}{\partial z}\rho-(\kappa+1)\frac{\partial^2\tilde{w}}{\partial z^2}=0.\end{aligned} \tag{2–5}$$

The general solution of Equation (2–5) can be written as

$$\begin{cases}\tilde{u}_1(z,\rho)=(A_1+zA_2)e^{-\rho z}+(A_3+zA_4)e^{\rho z}, & (z\ge 0),\\ \tilde{w}_1(z,\rho)=\left[A_1+\left(\frac{\kappa}{\rho}+z\right)A_2\right]e^{-\rho z}+\left[-A_3+\left(\frac{\kappa}{\rho}-z\right)A_4\right]e^{\rho z}, & (z\ge 0),\end{cases}$$
$$\begin{cases}\tilde{u}_2(z,\rho)=(A_5+zA_6)e^{\rho z}, & (z\le 0),\\ \tilde{w}_2(z,\rho)=\left[-A_5+\left(\frac{\kappa}{\rho}-z\right)A_6\right]e^{\rho z}, & (z\le 0),\end{cases} \tag{2–6}$$

where the subscripts 1 and 2 of $\tilde{u}$ and $\tilde{w}$ label the regions $z \ge 0$ and $z < 0$, respectively, and A_α ($\alpha = 1, \ldots, 6$) are integral constants to be determined from the specific boundary conditions and the continuity conditions. We could obtain expressions for the stress and strain fields by substituting the above solutions into Equation (2–2) and using Hooke's law. We omit these for short. However, the stresses on the crack

surfaces are

$$\begin{aligned}\sigma_{rz}(r,0^-) &= \mu\int_0^\infty \left[2\rho^2 J_1(r\rho)A_5 + \rho J_1(r\rho)(1-\kappa)A_6\right]d\rho,\\ \sigma_{zz}(r,0^-) &= -\int_0^\infty \rho J_0(r\rho)\left[2\mu\rho A_5 + (\lambda+2\mu)(1-\kappa)A_6\right]d\rho,\end{aligned} \tag{2–7}$$

where λ and μ are the Lame's constants of elasticity.

Now, define two dislocation density functions $g_1(r)$ and $g_2(r)$ associated with the crack opening displacements by

$$g_1(r) = \frac{\partial}{\partial r}(w_1 - w_2)\big|_{z=0}, \qquad g_2(r) = \frac{1}{r}\frac{\partial}{\partial r}(ru_1 - ru_2)\big|_{z=0}. \tag{2–8}$$

We noted that the displacement w has its maximum at the center of the crack, and u is continuous at the crack tip. Therefore, g_1 and g_2 must satisfy the following auxiliary conditions:

$$g_1(r)\big|_{r=0} = 0, \qquad \int_0^c r g_2(r)dr = 0. \tag{2–9}$$

For the crack configuration in Figure 1, the free surface of the semiinfinite body is traction-free and the crack is subjected to an internal pressure p. Thus, the boundary conditions are

$$\begin{aligned}\sigma_{rz}(r,h) &= 0, & \sigma_{zz}(r,h) &= 0, \quad (0<r<\infty)\\ \sigma_{rz}(r,0^+) &= \sigma_{rz}(r,0^-) = 0, & \sigma_{zz}(r,0^+) &= \sigma_{zz}(r,0^-) = -p, \quad (r<c).\end{aligned} \tag{2–10}$$

In addition, the continuity conditions of stresses and displacements at $z = 0$ require that

$$\begin{aligned}\sigma_{rz}(r,0^+) &= \sigma_{rz}(r,0^-),\\ \sigma_{zz}(r,0^+) &= \sigma_{zz}(r,0^-),\\ u(r,0^+) &= u(r,0^-),\\ w(r,0^+) &= w(r,0^-),\end{aligned} \tag{2–11}$$

for $r \geq c$. Using Equations (2–6)–(2–11), the parameters A_5 and A_6 become

$$A_5 = \frac{\Delta_{11}X + \Delta_{12}Y}{\Delta}, \qquad A_6 = \frac{\Delta_{21}X + \Delta_{22}Y}{\Delta}, \tag{2–12}$$

where

$$\Delta = 8\rho^3(\kappa-1)(1-\kappa^2)(\lambda+\mu)(\lambda+2\mu)e^{2\rho h},$$

$$\Delta_{11} = 4\rho^2(\kappa-1)(\lambda+2\mu)\Big[(e^{2\rho h}-1)(\kappa-1)^2(\lambda+\mu)+4\mu\rho h(1-\kappa)+8\mu\rho^2h^2\Big],$$

$$\Delta_{12} = 4\rho^2(1+\kappa)\Big[(e^{2\rho h}-1)(\kappa-1)^2(\lambda+\mu)(\lambda+2\mu)-4\lambda\mu\rho h(1-\kappa)-8\mu^2\rho h(1-\kappa)-8\mu^2\rho^2h^2\Big],$$

$$\Delta_{21} = 8\rho^3(\kappa-1)(\lambda+2\mu)\big[(e^{2\rho h}-1)(\kappa-1)(\lambda+\mu)-4\mu\rho h\big],$$

$$\Delta_{22} = 8\rho^3\mu(1+\kappa)\big[(e^{2\rho h}-1)(\kappa-1)(\lambda+\mu)+4\mu\rho h\big],$$

and

$$X = \int_0^\infty r g_1(r) J_1(\rho r)dr, \qquad Y = \int_0^\infty r g_2(r) J_0(\rho r)dr. \tag{2–13}$$

Substituting Equation (2–12) into (2–7) and using the following relation of Bessel functions

$$\int_0^\infty \rho J_0(\rho r)J_1(\rho s)d\rho = -\frac{1}{\pi}\left[\frac{1}{s-r}+\frac{1}{s+r}+\frac{2M(s,r)-2s}{s^2-r^2}\right], \tag{2–14}$$

we obtain the singular integral equations

$$\begin{aligned}\frac{\mu}{2\pi(1-\nu)}\int_0^c\left[\frac{1}{s-r}+\frac{1}{s+r}+\frac{M_1(s,r)-1}{s-r}+\frac{M_1(s,r)-1}{s+r}\right]g_1(s)ds\\ +\int_0^c D_{11}(s,r)g_1(s)ds+\int_0^c D_{12}(s,r)g_2(s)ds\\ =\sigma_{zz}(r,0^-)=-p,\ \text{for } 0<r<c,\end{aligned}$$

$$\begin{aligned}\frac{\mu}{2\pi(1-\nu)}\int_0^c\left[\frac{1}{s-r}-\frac{1}{s+r}+\frac{M_2(s,r)-1}{s-r}-\frac{M_2(s,r)-1}{s+r}\right]g_2(s)ds\\ +\int_0^c D_{21}(s,r)g_1(s)ds+\int_0^c D_{22}(s,r)g_2(s)ds\\ =\sigma_{rz}(r,0^-)=0,\ \text{for } 0<r<c,\end{aligned} \tag{2–15}$$

where

$$M(s,r)=\begin{cases}\dfrac{r}{s}E(r/s), & \text{for } r<s,\\ \dfrac{r^2}{s^2}E(r/s)-\dfrac{r^2-s^2}{s^2}K(r/s), & \text{for } r>s,\end{cases} \tag{2–16}$$

$$
\begin{aligned}
D_{11}(r,s) &= -s\int_0^\infty \left(\frac{-2\mu\rho\Delta_{11}+(\lambda+2\mu)(\kappa-1)\Delta_{21}}{\Delta}+\frac{\mu}{2(1-\nu)}\right)\rho J_0(\rho r)J_1(\rho s)d\rho,\\
D_{12}(r,s) &= -s\int_0^\infty \frac{-2\mu\rho\Delta_{12}+(\lambda+2\mu)(\kappa-1)\Delta_{22}}{\Delta}\rho J_0(\rho r)J_1(\rho s)d\rho,\\
D_{21}(r,s) &= -\mu s\int_0^\infty \frac{2\rho\Delta_{11}+(1-\kappa)\Delta_{21}}{\Delta}\rho J_1(\rho r)J_1(\rho s)d\rho,\\
D_{22}(r,s) &= s\int_0^\infty \left[\mu\frac{2\rho\Delta_{12}+(1-\kappa)\Delta_{22}}{\Delta}+\frac{\mu}{2(1-\nu)}\right]\rho J_1(\rho r)J_0(\rho s)d\rho,
\end{aligned}
\tag{2–17}
$$

with $K(x)$ and $E(x)$ being the elliptical integrals of the first and the second kind.

We next adopt dimensionless variables $t=(2s-c)/c$ and $x=(2r-c)/c$, and Equation (2–15) becomes

$$
\begin{aligned}
&\frac{\mu}{2\pi(1-\nu)}\int_{-1}^{1}\left[\frac{1}{t-x}+\frac{1}{t+x+2}+\frac{M_1(t,x)-1}{t-x}+\frac{M_1(t,x)-1}{t+x+2}\right]g_1(t)dt\\
&\qquad+\int_{-1}^{1}D_{11}(t,x)g_1(t)\frac{c}{2}dt+\int_{-1}^{1}D_{12}(t,x)g_2(t)\frac{c}{2}dt=-p, \qquad \text{for } -1<t<1,\\
&\frac{\mu}{2\pi(1-\nu)}\int_{-1}^{1}\left[\frac{1}{t-x}-\frac{1}{t+x+2}+\frac{M_2(t,x)-1}{t-x}-\frac{M_2(t,x)-1}{t+x+2}\right]g_2(t)dt\\
&\qquad+\int_{-1}^{1}D_{21}(t,x)g_1(t)\frac{c}{2}dt+\int_{-1}^{1}D_{22}(t,x)g_2(t)\frac{c}{2}dt=0, \qquad \text{for } -1<t<1.
\end{aligned}
\tag{2–18}
$$

Let us assume

$$
H_1(t)=g_1(t)\sqrt{1-t^2}, \qquad H_2(t)=g_2(t)\sqrt{1-t^2}. \tag{2–19}
$$

To solve the singular integral equations in Equation (2–9), expand the functions $H_1(t)$ and $H_2(t)$ in series

$$
H_1(t)=\sum_{n=0}^{\infty}A_nT_n(t), \qquad H_2(t)=\sum_{n=0}^{\infty}B_nT_n(t), \tag{2–20}
$$

where $T_n(t)$ is the Chebyshev polynomial of the first kind. Then, after truncating the series after N terms, Equations (2–18) and (2–9) become

$$\begin{aligned}
&\frac{\mu}{2(1-\nu)}\sum_{\alpha=1}^{N}\left[\frac{1}{t_\alpha - x_m}+\frac{1}{t_\alpha + x_m + 2}+\frac{M_1(t_\alpha, x_m)-1}{t_\alpha - x_m}\right.\\
&\qquad\left.+\frac{M_1(t_\beta, x_m)-1}{t_\beta + x_m + 2}+\frac{\pi c}{2}D_{11}(t_\beta, x_m)\right]\frac{H_1(t_l)}{N}+\sum_{\beta=1}^{N}\frac{\pi c}{2}D_{12}(t_\beta, x_j)H_2(t_\beta)=-p,\\
&\frac{\mu}{2(1-\nu)}\sum_{\alpha=1}^{N}\left[\frac{1}{t_\alpha - x_j}-\frac{1}{t_\alpha + x_j + 2}+\frac{M_2(t_\alpha, x_j)-1}{t_\alpha - x_j}\right.\\
&\qquad\left.-\frac{M_2(t_\alpha, x_j)-1}{t_\alpha + x_j + 2}+\frac{\pi c}{2}D_{22}(t_\alpha, x_j)\right]\frac{H_2(t_\alpha)}{N}+\sum_{\beta=1}^{N}\frac{\pi c}{2}D_{21}(t_\beta, x_m)\frac{H_1(t_\beta)}{N}=0,\\
&H_1(t_N)=0,\\
&\sum_{\beta=1}^{N}\frac{1+t_\beta}{2}H_1(t_\beta)=0,
\end{aligned}\tag{2–21}$$

where t_α and x_m are defined by

$$\begin{aligned}
t_\alpha &= \cos\frac{2\alpha-1}{2N} \qquad (l=1,\ldots,N),\\
x_m &= \cos\frac{m\pi}{N} \qquad (m=1,\ldots,N-1).
\end{aligned}\tag{2–22}$$

The system (2–21) comprises $2N$ linear algebraic equations in $2N$ unknowns $H_1(t_\alpha)$ and $H_2(t_\alpha)$. They can be solved numerically. By increasing N, the result tends to the exact solution; in our experience, some 50 terms yield a highly accurate solution. In this way, the stresses, strains, and displacements in the crack system can all be determined.

Finally, using the definitions of the mode-I and mode-II SIFs, we find

$$\begin{aligned}
K_{\mathrm{I}} &= \lim_{r\to c^+}\sqrt{2\pi(r-c)}\sigma_{zz}(r,0)=-\frac{\mu c\sqrt{\pi}}{2\sqrt{2}(1-\nu)}H_1(1),\\
K_{\mathrm{II}} &= \lim_{r\to c^+}\sqrt{2\pi(r-c)}\sigma_{rz}(r,0)=-\frac{\mu c\sqrt{\pi}}{2\sqrt{2}(1-\nu)}H_2(1).
\end{aligned}\tag{2–23}$$

In Figure 2, we illustrate. For the circular subsurface crack subjected to an internal pressure p (Figure 1), we plot both the mode-I and mode-II SIFs K_{I} and K_{II} as a function of c/h, the ratio between the crack radius and its distance from the upper surface. The reference value $K_0 = 2p\sqrt{c/\pi}$ is the mode-I SIF of a circular crack embedded in an infinite body (that is, $c/h \to 0$) and subjected to internal pressure p. For a fixed crack size c, both the absolute values of K_{I} and K_{II} vary against increasing relative depth, h/c. For a crack near the free surface of a semiinfinite body, K_{II} is relatively high because the crack interacts with the surface. For a deeply embedded crack (that is, $c/h \to 0$), K_{I} tends to K_0, and K_{II} is

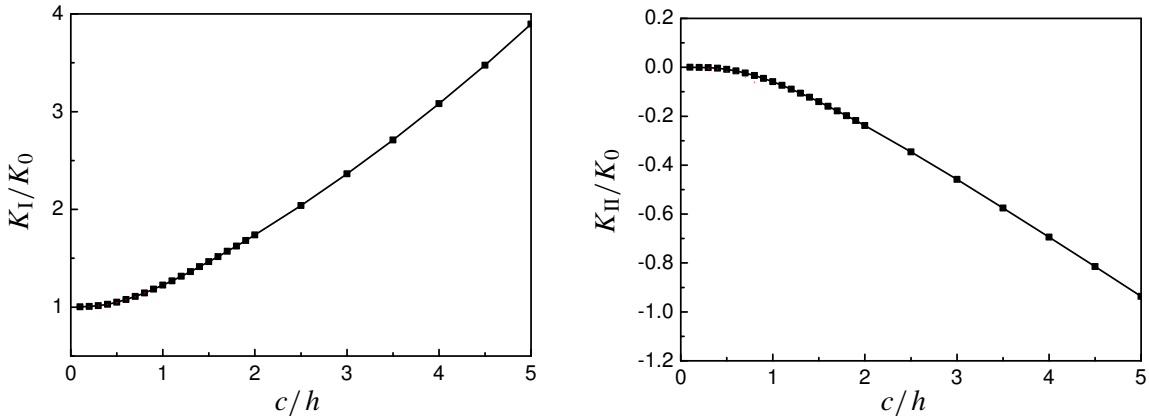

Figure 2. SIFs of a circular subsurface crack under internal pressure.

negligible. Also, for a very large ratio c/h, the aperture's square root tip behavior is confined to a very small region. For more detailed discussion of the asymptote's changing nature, the reader may refer to [Dyskin et al. 2000]. Additionally, we note that the values of K_{II} in Figure 2 differ by a factor of about 2 from those of [Bunger and Detournay 2005], while the respective values of K_I agree, approximately. We attribute the discrepancy to Bunger and Detournay [2005]'s assumption of a linear distribution of radial stress, which is not exact near the crack front at the plate boundary.

2.2. ***Plane strain problems.*** To illustrate plane strain problems, we consider a semiinfinite body containing a straight planar crack in parallel with the upper surface and subjected to an internal pressure p. Establish a Cartesian coordinate system $(o-xyz)$, as shown in Figure 3. The crack has length $2c$ in the x-direction and is infinite in the z-direction. The stress equilibrium equations are satisfied automatically when the stress components are expressed from the Airy stress function F as

$$\sigma_{xx} = \frac{\partial^2 F}{\partial y^2}, \qquad \sigma_{yy} = \frac{\partial^2 F}{\partial x^2}, \qquad \sigma_{xy} = -\frac{\partial^2 F}{\partial x \partial y}. \tag{2–24}$$

Substituting Equation (2–24) into the isotropic elastic constitutive relations and the result into the strain compatibility condition, we find that F must satisfy the biharmonic equation

$$\nabla^2 \nabla^2 F(x, y) = 0. \tag{2–25}$$

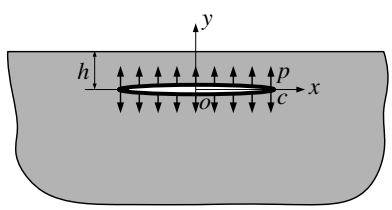

Figure 3. A subsurface Griffith crack beneath the free surface of a semiinfinite body.

For Section 2.1's axisymmetrical case, we used the Hankel transform. For plane strain problems, we use the Fourier transform instead. After Fourier transforming in x, Equation (2–25) becomes an ordinary differential equation

$$\frac{d^4}{dy^4}\widetilde{F} - 2\xi^2\frac{d^2}{dy^2}\widetilde{F} + \xi^4\widetilde{F} = 0. \tag{2–26}$$

It has the general solution

$$\widetilde{F}_1 = A_1 e^{|\xi|y} + A_2 y e^{|\xi|y} + A_3 e^{-|\xi|y} + A_4 y e^{-|\xi|y}, \quad \text{for } y \geq 0, \tag{2–27}$$

$$\widetilde{F}_2 = A_5 e^{|\xi|y} + A_6 y e^{|\xi|y}, \qquad \text{for } y < 0, \tag{2–28}$$

where A_α $(\alpha = 1, \ldots, 6)$ are integral constants as before.

Analogously to Equation (2–8), we define two dislocation density functions $g_{i=1,2}(x)$,

$$g_i(x) = \frac{\partial}{\partial x}\left[u_i(x, 0^+) - u_i(x, 0^-)\right], \tag{2–29}$$

where $u_i(x, y)$, $i = 1, 2$ denote the displacement components in the x- and y-directions, respectively. The $g_i(x)$ satisfy the auxiliary conditions

$$\int_{-c}^{c} g_i(x)dx = 0. \tag{2–30}$$

As we did in Equation (2–18), we then derive the following singular integral equations for the crack configuration in Figure 3:

$$\begin{aligned}
&\frac{\mu}{2\pi(1-\nu)}\left[-c\int_{-1}^{+1} D_{11}(t,r)g_1(t)dt + \int_{-1}^{+1}\frac{g_1(t)}{t-r}dt - 2c\int_{-1}^{+1} D_{12}(t,r)g_2(t)dt\right] = -p,\\
&\frac{\mu}{2\pi(1-\nu)}\left[-c\int_{-1}^{+1} D_{22}(t,r)g_2(t)dt + \int_{-1}^{+1}\frac{g_2(t)}{t-r}dt + 2c\int_{-1}^{+1} D_{21}(t,r)g_1(t)dt\right] = 0,
\end{aligned} \tag{2–31}$$

where $t = x/c$ is the dimensionless coordinate in the x-direction, and

$$\begin{aligned}
D_{11}(t,r) &= \int_0^{+\infty} (1 + 2\xi h + 2\xi^2 h^2)e^{-2\xi h}\sin\xi[(t-r)c]d\xi,\\
D_{12}(t,r) = D_{21}(t,r) &= \int_0^{+\infty} \xi^2 h^2 e^{-2\xi h}\cos\xi[(t-r)c]d\xi,\\
D_{22}(t,r) &= \int_0^{+\infty} (1 - 2\xi h + 2\xi^2 h^2)e^{-2\xi h}\sin\xi[(t-r)c]d\xi.
\end{aligned} \tag{2–32}$$

Now define $H_{i=1,2}$ by $H_i(t) = g_i(t)\sqrt{1-t^2}$. By expanding $H_i(t)$ as a truncated series of first kind Chebyshev polynomials, as in Equation (2–20), we obtain the system of linear equations

$$\frac{\mu}{2(1-\nu)}\left[-c\sum_{l=1}^{N} D_{11}(t_l, x_m)\frac{H_1(t_l)}{N} + \sum_{l=1}^{N}\frac{H_1(t_l)}{N(t_i, x_j)} - 2c\sum_{i=1}^{N} D_{12}(t_i, x_j)\frac{H_2(t_i)}{N}\right] = -p,$$

$$\frac{\mu}{2(1-\nu)}\left[-c\sum_{i=1}^{N} D_{22}(t_i, x_j)\frac{H_2(t_i)}{N} + \sum_{i=1}^{N}\frac{H_2(t_i)}{N(t_i - x_j)} + 2c\sum_{l=1}^{N} D_{21}(t_l, x_m)\frac{H_1(t_l)}{N}\right] = 0,$$

$$\sum_{l=1}^{N} H_i(t_l) = 0, \tag{2–33}$$

These we solve easily using numerical matrix methods, and hence determine the fields of stresses, strains and displacements.

Finally, the SIFs are

$$K_{\mathrm{I}} = \lim_{x\to c^+}\sqrt{2\pi(x-c)}\sigma_y(x,0) = \lim_{r\to 1^+}\sqrt{\pi c(r-1)}\int_{-1}^{+1}\frac{g(s)}{s-r}ds = \alpha\sqrt{\pi c}H_1(1) \tag{2–34}$$

$$K_{\mathrm{II}} = \lim_{x\to c^+}\sqrt{2\pi(x-c)}\tau_{xy}(x,0) = \lim_{r\to 1^+}\sqrt{\pi c(r-1)}\int_{-1}^{+1}\frac{f(s)}{s-r}ds = \alpha\sqrt{\pi c}H_2(1). \tag{2–35}$$

We plot the calculated K_{I} and K_{II} in Figure 4, where $K_0 = p\sqrt{\pi c}$ is the SIF of a Griffith crack in an infinite solid and subjected to an internal pressure p. Both the absolute values of K_{I} and K_{II} increase with c/h. For a deeply embedded crack (that is, $c/h \to 0$), K_{I} and K_{II} tend to K_0 and zero.

Another important plane strain problem consists of a semiinfinite body containing a periodic array of interacting Griffith cracks in parallel with the upper surface and subjected to a uniform internal pressure

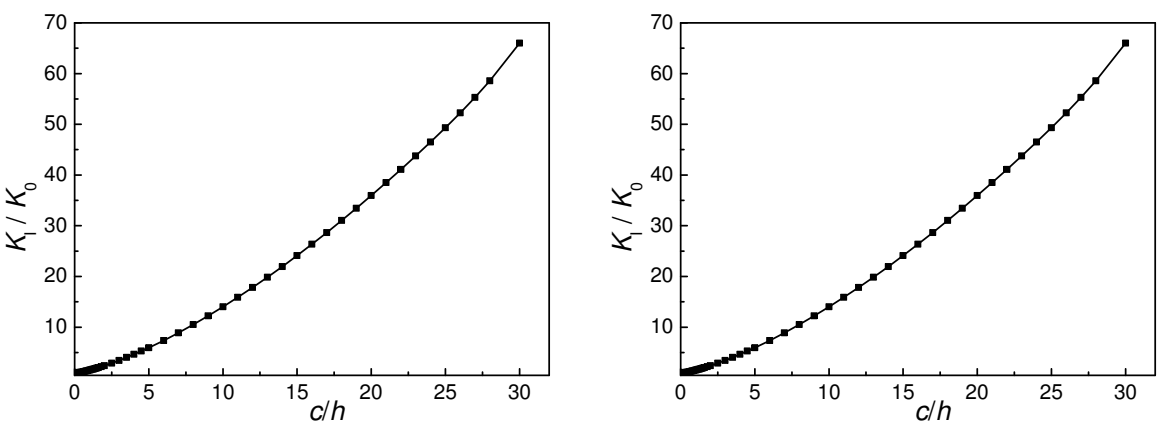

Figure 4. SIFs of a subsurface Griffith crack, (a) K_{I} and (b) K_{II}.

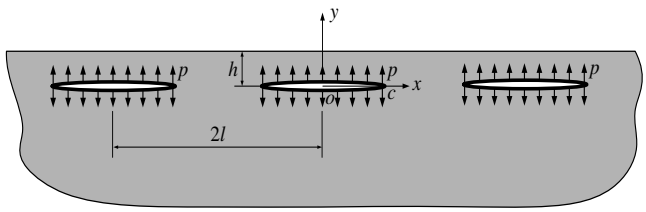

Figure 5. A periodic array of plane-strain subsurface Griffith cracks.

p, as shown in Figure 5. All cracks have length $2c$, and the spacing between neighboring cracks is $2l$. The singular integral transform method described above extends readily to this problem. Omitting the detailed derivation, this problem reduces to solving the singular integral equations

$$\frac{\mu}{2(1-\nu)}\left\{-\frac{1}{\pi}\int_{-c}^{+c}\left[D_{11}^{0}+\sum_{n=1}^{a_0}(D_{11}^{-}+D_{11}^{+})\right]g_1(t)dt+\frac{1}{2l}\int_{-c}^{+c}\operatorname{cotan}\left(\pi\frac{t-x}{2l}\right)g_1(t)dt\right.$$
$$\left.-\frac{2}{\pi}\int_{-c}^{+c}\left[D_{12}^{0}+\sum_{n=1}^{a_0}(D_{12}^{-}+D_{12}^{+})\right]g_2(t)dt\right\}=-p,$$

$$\frac{\mu}{2(1-\nu)}\left\{-\frac{1}{\pi}\int_{-c}^{+c}\left[D_{22}^{0}+\sum_{n=1}^{a_0}\left(D_{22}^{-}+D_{22}^{+}\right)\right]g_2(t)dt+\frac{1}{2l}\int_{-c}^{+c}\operatorname{cotan}\left(\pi\frac{t-x}{2l}\right)g_2(t)dt\right.$$
$$\left.+\frac{2}{\pi}\int_{-c}^{+c}\left[D_{21}^{0}+\sum_{n=1}^{a_0}\left(D_{21}^{-}+D_{21}^{+}\right)\right]g_1(t)dt\right\}=0, \quad (2\text{–}36)$$

where

$$D_{11}^{0}(t,x)=D_{11}(t,x),\qquad D_{12}^{0}(t,x)=D_{12}(t,x),\qquad D_{22}^{0}(t,x)=D_{22}(t,x),$$
$$D_{11}^{\pm}(t,x)=\int_{0}^{+\infty}(1+2\xi h+2\xi^2h^2)e^{-2\xi h}\sin\xi(t-x\pm 2nl)d\xi,$$
$$D_{12}^{\pm}(t,x)=D_{21}^{\pm}+(t,x)=\int_{0}^{+\infty}\xi^2h^2e^{-2\xi h}\cos\xi(t-x\pm 2nl)d\xi, \quad (2\text{–}37)$$
$$D_{22}^{\pm}(t,x)=\int_{0}^{+\infty}(1-2\xi h+2\xi^2h^2)e^{-2\xi h}\sin\xi(t-x\pm 2nl)d\xi.$$

We show the calculated mode-I and mode-II SIFs K_{I} and K_{II} in Figure 6. For a small crack spacing in the range $1<l/c<2$, crack interaction significantly influences the SIF solutions. For a larger spacing $l/c>3$, the interaction effect is negligible, and the SIFs tend to the solutions for a single crack, shown in

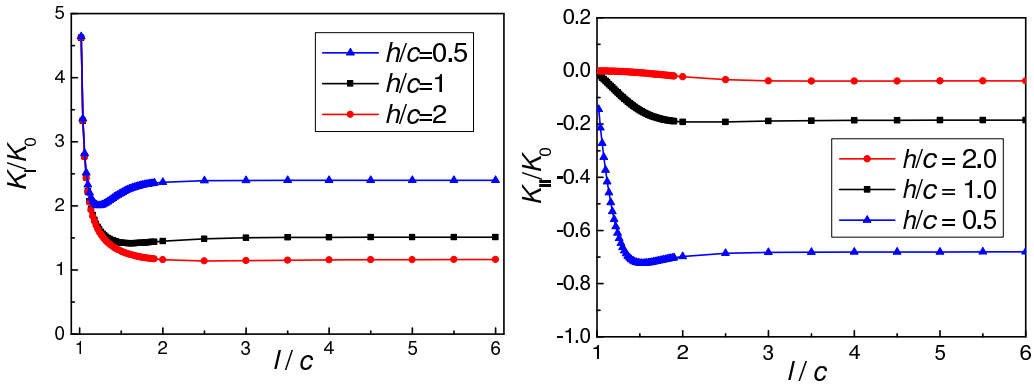

Figure 6. SIFs of a periodic array of subsurface cracks, (a) K_{I} and (b) K_{II}.

Figure 3. In addition, the crack interaction may shield the SIFs under some combinations of geometric parameters (for example, in the range $1.2 < l/c < 1.6$ with $h/c = 0.5$, as shown in Figure 6), though the interaction effect usually enhances the SIFs [Feng and Yu 2002].

3. Analysis of three-dimensional ion cut

As mentioned in the introduction, the Smart-Cut technology allows production of various SOI wafers with highly uniform thickness. However, metal wires and distributed device elements in integrated circuits require imposing patterns, for example, straight grooves and circular holes, on wafer surfaces. Here, we suggest using the ion cut method to carve three-dimensional surface directly. See Figure 7 for a schema of the basic procedure. The wafer is covered with a specialized metal mask and exposed to an appropriate dose of hydrogen ions at room-temperature [Feng and Huang 2004]. The mask's holes conform to the required wafer surface pattern, and it is thick enough so that hydrogen ions cannot pass

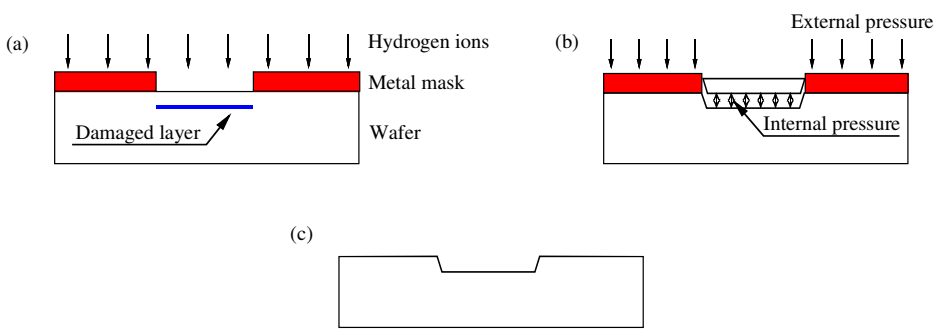

Figure 7. Schematics of the three-dimensional ion cut method: (a) hydrogen ion implantation, (b) thermal annealing and wafer splitting, and (c) the final wafer with a designed surface pattern.

through it, ensuring that hydrogen ions are implanted only in the holes. The masked wafer is next exposed to thermal annealing including two stages of heating, a medium-temperature stage (400–600° C) and a high-temperature stage (about 1100° C). Pressure applied to the mask controls the crack propagation path. During the first stage of annealing, a thin damaged layer appears at the depth of the maximum hydrogen ion concentration. The cracks propagate by kinks, which form as microcrack coalesce within the damaged layer. This removes the unwanted material and creates the desired surface morphology. The subsequent high-temperature thermal treatment removes the remaining hydrogen ions and radiation defects.

Repeating the integral transform methods of Section 2, we next analyze the kink propagation of subsurface cracks and subsequent creation of several representative surface patterns, including shallow circular holes and straight grooves.

3.1. ***Ion cut of a circular hole.*** To determine how kinks propagate in a mixed-mode crack, we adopt the following fracture criterion, based on the maximum circumferential tensile stress [Lawn 1993]:

$$\frac{1}{2}\left[K_{\mathrm{I}}(1+\cos\alpha)-3K_{\mathrm{II}}\sin\alpha\right]\cos\frac{\alpha}{2}=K_{Ic}, \tag{3–1}$$

where K_{Ic} is the fracture toughness of the material, and α is the kinking angle measured from the crack direction. In the stress fields of a mixed-mode crack, the angle α is determined from

$$K_{\mathrm{I}}\sin\alpha+K_{\mathrm{II}}(3\cos\alpha-1)=0. \tag{3–2}$$

For the configuration in Figure 1, where the upper surface of the system is traction free and the crack is subjected to an internal pressure, the mode-II SIF K_{II} is generally much smaller than that of K_{I}. Substituting the calculated values for K_{I} and K_{II} values (in Figure 2) into Equation (3–2), we conclude that the kinking angle α is generally smaller than 25° if the upper surface of the body is traction free. Therefore, external surface pressure is necessary to produce a hole with a greater α value. Such pressure, applied through the metal mask, can be modeled either as a linear force q distributed along a circle (Figure 8a) or as a distributed surface force. We present only the first case here due to its particular significance, but the second case proceeds similarly.

According to the superposition principle, the crack problem in Figure 8(a) decomposes into sum of the two subproblems of Figures 8(b) and 8(c). In the first, the semiinfinite body has no crack but is subjected to the distributed force q along a circle on the upper surface. The corresponding stress fields can be derived from the well-known Boussinesq solution as

$$\begin{aligned}\bar{\sigma}_{zz}(r,0)&=-\frac{3ql_0h^3}{\pi}\int_0^{\pi}\frac{d\theta}{\left(l_0^2+r_0^2-2l_0r\cos\theta+h^2\right)^{5/2}},\\ \bar{\tau}_{zr}(r,0)&=-\frac{3ql_0h^2}{\pi}\int_0^{\pi}\frac{(l_0\cos\theta-r)d\theta}{\left(l_0^2+r^2-2l_0r\cos\theta+h^2\right)^{5/2}},\end{aligned} \tag{3–3}$$

where c is the crack radius, l_0 the radius where the linear force q is applied, and h is the distance of the crack from the upper surface. Other axisymmetric problems of a semiinfinite body subjected to surface forces can be solved easily by integrating the stress fields in Equation (3–3). In the second subproblem

(Figure 8c), the upper surface of the body is traction free but the crack surfaces are subjected to the tractions

$$\sigma_{zz}(r,0) = -\bar{\sigma}_{zz}(r,0) - p = \frac{3ql_0h^3}{\pi}\int_0^\pi \frac{d\theta}{\left(l_0^2 + r_0^2 - 2l_0 r\cos\theta + h^2\right)^{5/2}} - p,$$
$$\tau_{zr}(r,0) = \bar{\tau}_{zr}(r,0) = \frac{3ql_0h^2}{\pi}\int_0^\pi \frac{(l_0\cos\theta - r)d\theta}{\left(l_0^2 + r^2 - 2l_0 r\cos\theta + h^2\right)^{5/2}}. \tag{3–4}$$

The two cracks in Figures 8(a) and 8(c) share SIF values, but we can solve latter problem more easily using the integral transform method in Section 2.1. Omitting the detailed derivation, we obtain a system of linear equations, similar to Equation (2–20):

$$\frac{\mu}{2(1-\nu)}\sum_{l=1}^{N}\left[\frac{1}{t_l - x_m} + \frac{1}{t_l + x_m + 2} + \frac{M_1(t_l,x_m)-1}{t_l - x_m} + \frac{M_1(t_l,x_m)-1}{t_l + x_m + 2} + \frac{\pi c}{2}D_{11}(t_l,x_m)\right]\frac{H_1(t_l)}{N}$$
$$+\sum_{i=1}^{N}\frac{\pi c}{2}D_{12}(t_i,x_j)H_2(t_i) = \frac{3ql_0h^3}{\pi}\int_0^\pi \frac{d\theta}{\left(l_0^2 + c^2x_m^2 - 2l_0 cx_m\cos\theta + h^2\right)^{5/2}} - p,$$

$$\frac{\mu}{2(1-\nu)}\sum_{i=1}^{N}\left[\frac{1}{t_i - x_j} - \frac{1}{t_i + x_j + 2} + \frac{M_2(t_i,x_j)-1}{t_i - x_j} - \frac{M_2(t_i,x_j)-1}{t_i + x_j + 2} + \frac{\pi c}{2}D_{22}(t_i,x_j)\right]\frac{H_2(t_i)}{N}$$
$$+\sum_{l=1}^{N}\frac{\pi c}{2}D_{21}(t_l,x_m)\frac{H_1(t_l)}{N} = \frac{3ql_0h^2}{\pi}\int_0^\pi \frac{(l_0\cos\theta - cx_j)d\theta}{\left(l_0^2 + c^2x_j^2 - 2l_0 cx_j\cos\theta + h^2\right)^{5/2}},$$

$$H_1(t_N) = 0,$$

$$\sum_{l=1}^{N}\frac{1+t_l}{2}H_1(t_l) = 0. \tag{3–5}$$

Using the calculated stress fields, we calculate the SIFs K_{I} and K_{II} using Equation (2–23), and plot the results in Figure 9 as linear functions of the loading ratio, $q/2cp$. The ratio of SIFs $K_{\mathrm{II}}/K_{\mathrm{I}}$ increases with the increase in the externally applied force q. In Figure 10, we show the kinking angle α as a function of $q/2cp$. One may control the propagating kink angle, and hence the shape of the hole, by adjusting the force q. A large kinking angle requires a sufficiently large q; however, since the mode-I SIF decreases linearly with q, the crack will close and cease to propagate if q is too large. We note that the internal pressure p depends mainly upon the dose of implanted hydrogen ions and the temperature [Feng and Huang 2004]. Therefore, in order to cut a circular hole, an appropriate force q should be chosen from Figure 10 to conform to the required hole depth. Finally, we note that the hole's diameter and depth is limited by the ion implantation machine to the order of microns. The hydrogen ion penetration depth varies approximately linearly with the implantation energy and does not depend on the implantation dose [Feng and Huang 2004].

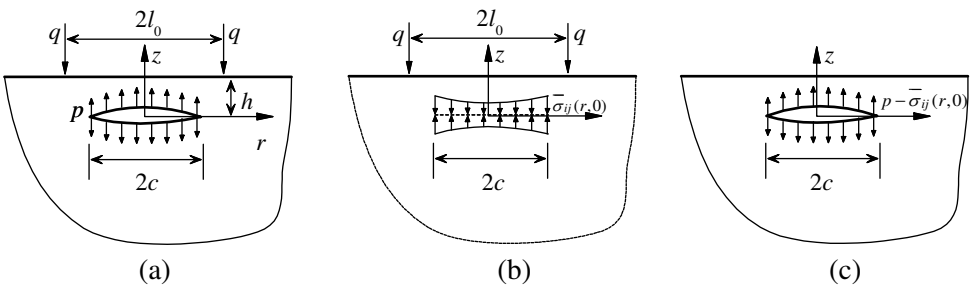

Figure 8. Superposition method for solving a subsurface crack.

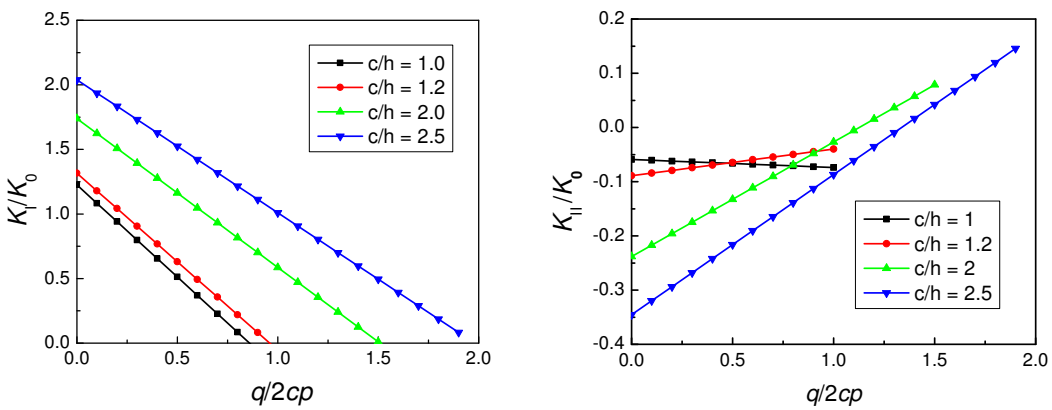

Figure 9. SIFs of a circular subsurface crack subjected to an internal pressure p and a surface force q, where $l_0 = 1.1c$. (a) K_{I} and (b) K_{II}.

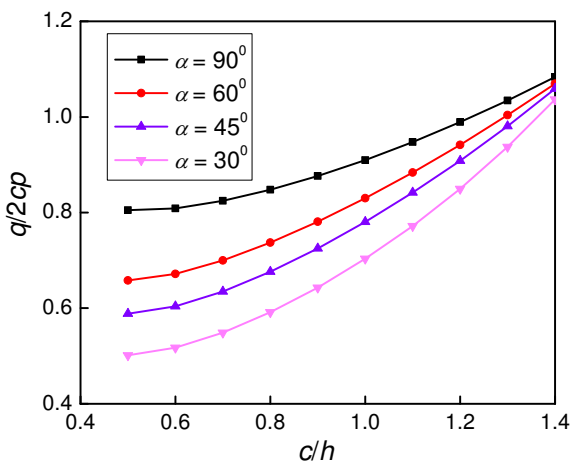

Figure 10. Kinking angle of a circular subsurface crack, where $l_0 = 1.1c$.

3.2. ***Ion cut of a long straight groove.*** To cut a long, straight surface groove on a wafer, hydrogen ions are implanted into a long square zone left uncovered by a metal mask. We assume that the groove is much longer than its width, c, so the ion cut process simplifies to a plane strain problem. The corresponding crack model can also represented by Figure 8, but without the same plane strain assumption. We again employ superposition. In this case, the tractions on the crack faces in Figure 8(c) become

$$\begin{aligned}\bar{\sigma}_{yy}(x,0) &= \frac{2qh^3}{\pi}\left\{\frac{1}{\left[h^2+(l_0+x)^2\right]^2}+\frac{1}{\left[h^2+(l_0-x)^2\right]^2}\right\}-p,\\ \bar{\tau}_{xy}(x,0) &= \frac{2qh^2}{\pi}\left\{\frac{l_0+x}{\left[h^2+(l_0+x)^2\right]^2}+\frac{x-l_0}{\left[h^2+(l_0-x)^2\right]^2}\right\},\end{aligned} \tag{3–6}$$

where q is the magnitude of the distributed force per unit length along the z-axis direction. In deriving Equation (3–6), we again used the Boussinesq solution under the plane strain condition [Timoshenko and Goodier 1970].

Substituting Equation (3–6) into the boundary conditions along the crack faces, we obtain the following singular integral equation system, similar to Equation (2–31):

$$\begin{aligned}&\frac{\mu}{2\pi(1-\nu)}\left[-c\int_{-1}^{+1}D_{11}(s,r)g_1(s)ds+\int_{-1}^{+1}\frac{g_1(s)}{s-r}ds-2c\int_{-1}^{+1}D_{12}(s,r)g_2(s)ds\right]\\ &\qquad=\frac{2qh^3}{\pi}\left\{\frac{1}{[h^2+(l_0+cr)^2]^2}+\frac{1}{[h^2+(l_0-cr)^2]^2}\right\}-p,\\ &\frac{\mu}{2\pi(1-\nu)}\left[-c\int_{-1}^{1}D_{22}(s,r)g_2(s)ds+\int_{-1}^{1}\frac{g_2(s)}{s-r}ds+2c\int_{-1}^{1}D_{21}(s,r)g_1(s)ds\right]\\ &\qquad=\frac{2qh^2}{\pi}\left\{\frac{l_0+cr}{[h^2+(l_0+cr)^2]^2}+\frac{cr-l_0}{[h^2+(l_0-cr)^2]^2}\right\},\\ &\int_{-1}^{+1}g_{1,2}(r)dr=0,\end{aligned} \tag{3–7}$$

which we solved easily using the method in Section 2.2. We plot the results for SIFs K_{I} and K_{II} and the kinking angle α in Figures 11 and 12. As for the circular hole, we find that both the SIF ratio $K_{\mathrm{II}}/K_{\mathrm{I}}$ and the kinking angle α increase with the externally applied force q. Therefore, one can direct propagating kinks by varying the force q. If $K_{\mathrm{I}} \le 0$, the crack will close, not propagate. This limits the kinking angle α to 70°, that is, the shape of the cut groove.

3.3. ***Ion cut of an array of periodic grooves.*** Finally, we analyze the ion cut method for an array of periodic long straight grooves. We model the ion cut process using the crack configuration in Figure 13. Here q is the distributed force per unit area. We solve by superposition, as shown analogously in

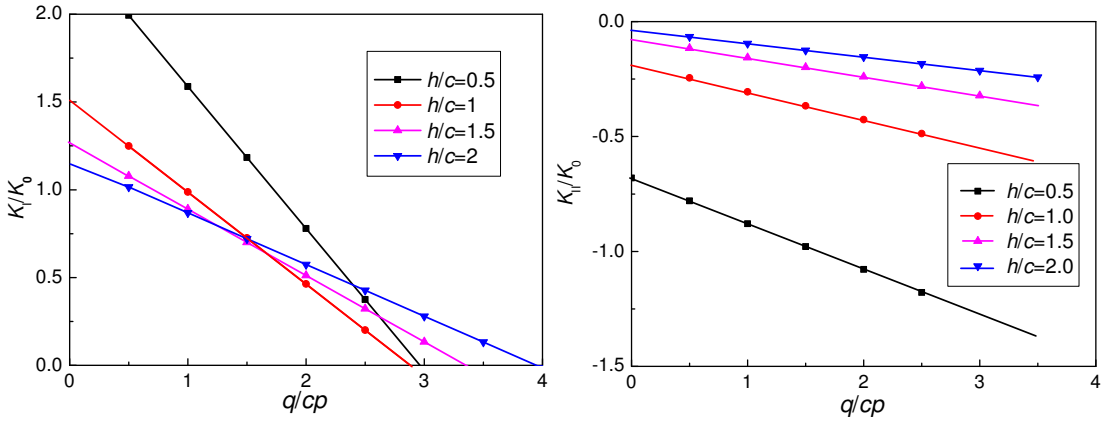

Figure 11. SIFs of a subsurface Griffith crack, (a) K_{I} and (b) K_{II}.

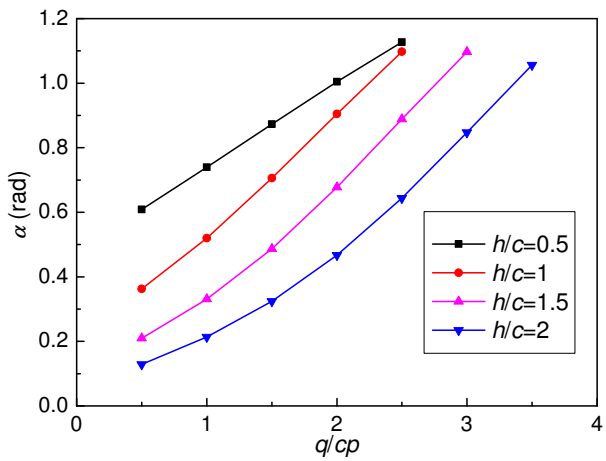

Figure 12. Kinking angle of a subsurface Griffith crack.

Figure 8. Accordingly, the crack SIFs in Figure 13 are those of a semiinfinite space, where the upper

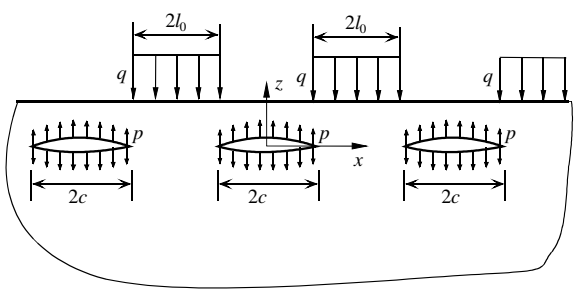

Figure 13. Crack model for cutting of a periodic array of straight grooves.

surface of the body is traction free and the tractions on the crack surfaces are given by

$$\bar{\sigma}_{yy}(x,0)=\frac{2qh^3}{\pi}\left\{\sum_{n=0}^{\infty}\int_{-2nl-a}^{-2(n+1)l+a}\frac{dx_2}{[(x-x_2)^2+h^2]^2}+\sum_{n=0}^{\infty}\int_{2nl+a}^{2(n+1)l-a}\frac{dx_2}{[(x-x_2)^2+h^2]^2}\right\}-p,$$
$$\bar{\tau}_{xy}(x,0)=-\frac{2qh^2}{\pi}\left\{\sum_{n=0}^{\infty}\int_{-2nl-a}^{-2(n+1)l+a}\frac{(x-x_2)dx_2}{[(x-x_2)^2+h^2]^2}+\sum_{n=0}^{\infty}\int_{2nl+a}^{2(n+1)l-a}\frac{(x-x_2)dx_2}{[(x-x_2)^2+h^2]^2}\right\}, \tag{3–8}$$

where we use again the plane-strain Boussinesq solution. The integral transform method leads to a singular integral equation system for the crack configuration in Figure 13:

$$\begin{aligned}-\alpha\Bigg(&-c\sum_{q=1}^{N_0}\left\{D_{11}^0(s_q,r_m)+\sum_{n=1}^{a_0}[D_{11}^-(s_q,r_m)+D_{11}^+(s_q,r_m)]\right\}\frac{H_1(s_q)}{N_0}\\&+\frac{\pi c}{2l}\sum_{q=1}^{N_0}\left[\cot\left(\pi\frac{s_q-r_m}{2l}c\right)-\frac{1}{\pi\frac{s_q-r_m}{2l}c}\right]\frac{H_1(s_q)}{N_0}+\sum_{q=1}^{N_0}\frac{H_1(s_q)}{(s_q-r_m)N_0}\\&-2c\sum_{i=1}^{N_0}\left\{D_{12}^0(s_i,r_m)+\sum_{n=1}^{a_0}[D_{12}^-(s_i,r_m)+D_{12}^+(s_i,r_m)]\right\}\frac{H_2(s_i)}{N_0}\Bigg)\\&=\frac{2qh^3}{\pi}\left\{\sum_{n=0}^{\infty}\int_{-2nl-c}^{-2(n+1)l+c}\frac{dx_2}{\left[(cr_m-x_2)^2+h^2\right]^2}+\sum_{n=0}^{\infty}\int_{2nl+c}^{2(n+1)l-c}\frac{dx_2}{\left[(cr_m-x_2)^2+h^2\right]^2}\right\}-p,\end{aligned}$$

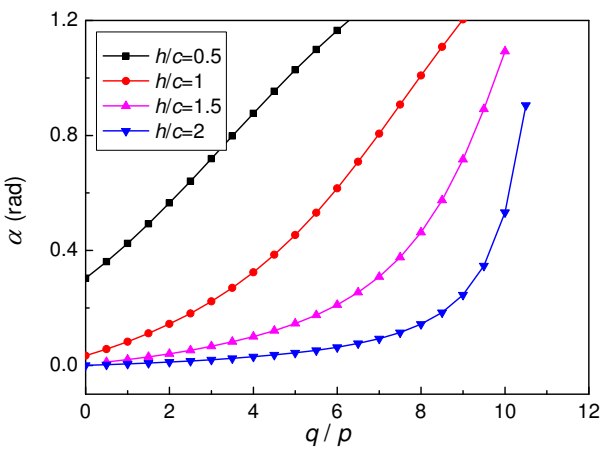

Figure 14. Kinking angle of a periodic array of subsurface cracks, where $l_0 = 1.1c$.

$$\alpha\left(-c\sum_{i=1}^{N_0}\left\{D_{22}^{0}(s_i,r_j)+\sum_{n=1}^{a_0}\left[D_{22}^{-}(s_i,r_j)+D_{22}^{+}(s_i,r_j)\right]\right\}\frac{H_2(s_i)}{N_0}\right.$$
$$+\frac{\pi c}{2l}\sum_{i=1}^{N_0}\left[\cot\left(\pi\frac{s_i-r_j}{2l}c\right)-\frac{1}{\pi\frac{s_i-r_j}{2l}c}\right]\frac{H_2(s_i)}{N_0}+\sum_{i=1}^{N_0}\frac{H_2(s_i)}{(s_i-r_j)N_0}$$
$$\left.+2c\sum_{q=1}^{N_0}\left\{D_{21}^{0}(s_q,r_j)+\sum_{n=1}^{a_0}\left[D_{21}^{-}(s_q,r_j)+D_{21}^{+}(s_q,r_j)\right]\right\}\frac{H_1(s_q)}{N_0}\right)$$
$$=\frac{2qh^2}{\pi}\left\{\sum_{n=0}^{\infty}\int_{-2nl-c}^{-2(n+1)l+c}\frac{(cr_j-x_2)dx_2}{\left[(cr_j-x_2)^2+h^2\right]^2}+\sum_{n=0}^{\infty}\int_{2nl+c}^{2(n+1)l-c}\frac{(cr_j-x_2)dx_2}{\left[(cr_j-x_2)^2+h^2\right]^2}\right\},$$

$$\sum_{l=1}^{N}H_1(t_l)=0,$$

$$\sum_{i=1}^{N}H_2(t_i)=0.$$

Thus we determine the stress fields and the SIFs K_{I} and K_{II}. For brevity, we plot in Figure 14 only the kinking angle α as a function of the loading ratio q/p. This function can be implicitly solved for q, so that, for a desired value of α and internal pressure p (determined by the dose of implanted hydrogen ions), we know the correct force q to apply.

4. Conclusions

We suggest using the ion cut technology to cut directly the surface patterns onto wafers bound for integrated circuits. In the present work, we analyzed the three-dimensional ion cut method using fracture mechanics theory and demonstrated that patterns can be transferred from a mask to an Si or SOI substrate. We presented a convenient method based on integral transforms for calculating the SIFs of subsurface cracks. The Hankel and Fourier integral transforms lent themselves to the axisymmetric and planar-symmetric crack configurations, respectively. Cracks near a surface are generally of mixed-mode because of the nonsymmetric geometry. We gave selected, important solutions for the SIFs of subsurface cracks, but the method can solve many other crack configurations. This method is comparatively easier than the finite element method, and yields the mode-I and II SIFs with higher accuracy. We analyzed the conditions for successfully using the three-dimensional ion cut method. An externally applied force is then required to cut the desired surface morphology. One may vary the kinking direction of subsurface cracks by specifying the ratio of the applied surface force and the internal pressure induced by the implanted hydrogen.

References

[Aspar et al. 1996] B. Aspar, M. Bruel, M. Zussy, and A. M. Cartier, "Transfer of structured and patterned thin silicon films using the Smart-Cut$^{(R)}$ process", *Electron. Lett.* **32**:21 (1996), 1985–1986.

[Aspar et al. 1999] B. Aspar, E. Jalaguier, A. Mas, C. Locatelli, O. Rayssac, S. Pocas, A. M. Papon, J. F. Michaud, and M. Bruel, "Smart-Cut$^{(R)}$ process using metallic bonding: application to transfer of Si, GaAs, InP thin films", *Electron. Lett.* **35**:12 (1999), 1024–1025.

[Bruel 1995] M. Bruel, "Silicon on insulator material technology", *Electron. Lett.* **31**:14 (1995), 1201–1202.

[Bruel 1996] M. Bruel, "Application of hydrogen ion beams to silicon on insulator material technology", *Nucl. Instrum. Meth. B* **108**:3 (1996), 313–319.

[Bunger and Detournay 2005] A. P. Bunger and E. Detournay, "Asymptotic solution for a penny-shaped near-surface hydraulic fracture", *Eng. Fract. Mech.* **72**:16 (2005), 2468–2486.

[Cao 2002] Y. Cao, "Three-dimensional finite element modeling of subsurface median crack in trilayer sandwiches due to contact loading", *Eng. Fract. Mech.* **69**:6 (2002), 729–743.

[Colinge 1991] J.-P. Colinge, *Silicon-on-insulator technology: materials to VLSI*, Kluwer, Boston, 1991.

[Di Cioccio et al. 1997] L. Di Cioccio, Y. LeTiec, C. Jaussaud, M. Bruel, and E. Hugonnard-Bruyere, "Silicon carbide on insulator formation by the Smart-Cut$^{(R)}$ process", *Mat. Sci. Eng. B* **46**:1-3 (1997), 349–356.

[Dyskin et al. 2000] A. V. Dyskin, L. N. Germanovich, and K. B. Ustinov, "Asymptotic analysis of crack interaction with free boundary", *Int. J. Solids Struct.* **37**:6 (2000), 857–886.

[Feng and Huang 2004] X.-Q. Feng and Y. Huang, "Mechanics of Smart-Cut$^{(R)}$ technology", *Int. J. Solids Struct.* **41**:16-17 (2004), 4299–4320.

[Feng and Xu 2006] X.-Q. Feng and M. Xu, "Solutions of stress intensity factors of subsurface cracks", *Key Eng. Mat.* **312** (2006), 83–88.

[Feng and Yu 2002] X. Q. Feng and S. W. Yu, *Damage micromechanics of quasi-brittle solids*, Tsinghua University Press, Beijing, 2002.

[Fleming and Suh 1977] J. R. Fleming and N. P. Suh, "Mechanics of cracks propagation in delamination wear", *Wear* **44**:1 (1977), 39–56.

[Gad et al. 2003] M. A. Gad, J. H. Evans-Freeman, N. Cinosi, and J. Sarma, "Loss measurements of er-doped silicon-on-insulator waveguides", *Mat. Sci. Eng. B* **105**:1-3 (2003), 79–82.

[Goshima and Soda 1997] T. Goshima and T. Soda, "Stress intensity factors of a subsurface crack in a semi-infinite body due to rolling/sliding contact and heat generation", *JSME Int. J. A. Solid Mech. M.* **40**:3 (1997), 263–270.

[Haisma and Spierings 2002] J. Haisma and G. A. C. M. Spierings, "Contact bonding, including direct-bonding in a historical and recent context of materials science and technology, physics and chemistry : historical review in a broader scope and comparative outlook", *Mat. Sci. Eng. R* **37**:1-2 (2002), 1–60.

[Hutchinson and Suo 1992] J. W. Hutchinson and Z. Suo, "Mixed-mode cracking in layered materials", *Adv. Appl. Mech.* **29** (1992), 63–191.

[Jalaguier et al. 1998] A. Jalaguier, B. Aspar, S. Pocas, J. F. Michaud, M. Zussy, A. M. Papon, and M. Bruel, "Transfer of 3 in gaas film on silicon substrate by proton implantation process", *Electron. Lett.* **34**:4 (1998), 408–409.

[Komvopoulos 1996] K. Komvopoulos, "Subsurface crack mechanisms under indentation loading", *Wear* **199**:1 (1996), 9–23.

[Lawn 1993] B. R. Lawn, *Fracture of brittle solids*, Cambridge University Press, Cambridge, 1993.

[Ma and Hwang 1996] C.-C. Ma and L.-R. Hwang, "Dynamic fracture analysis of an inclined subsurface crack subjected to dynamic moving loadings", *Int. J. Fracture* **80**:1 (1996), 1–18.

[Ma et al. 2005] L. Ma, X. Wang, X.-Q. Feng, and S.-W. Yu, "Numerical analysis of interaction and coalescence of numerous microcracks", *Eng. Fract. Mech.* **72**:12 (2005), 1841–1865.

[Spence and Sharp 1985] D. A. Spence and P. W. Sharp, "Self-similar solutions for elastohydrodynamic cavity flow", *P. Roy. Soc. Lond. A Mat.* **400**:1819 (1985), 289–313.

[Srivastava and Singh 1969] K. N. Srivastava and K. Singh, "The effect of penny-shaped crack on the distribution of stress in a semi-infinite solid", *Int. J. Eng. Sci.* **7**:5 (1969), 469–490.

[Timoshenko and Goodier 1970] S. P. Timoshenko and J. N. Goodier, *Theory of elasticity*, 3rd ed., McGraw-Hill, New York, 1970.

[Tong and Bower 1998] Q.-Y. Tong and R. W. Bower, "Beyond "Smart-Cut$^{(R)}$": recent advances in layer transfer for material integration", *MRS Bull.* **23**:12 (1998), 40–44.

[Zhang et al. 2002] X. Zhang, E. Detournay, and R. Jeffrey, "Propagation of a penny-shaped hydraulic fracture parallel to the free-surface of an elastic half-space", *Int. J. Fracture* **115**:2 (2002), 125–158.

[Zhang et al. 2005] X. Zhang, R. G. Jeffrey, and E. Detournay, "Propagation of a hydraulic fracture parallel to a free surface", *Int. J. Numer. Anal. Met.* **29**:13 (2005), 1317–1340.

Received 23 Aug 2006. Revised 23 Jun 2007. Accepted 3 Jul 2007.

XI-QIAO FENG: fengxq@tsinghua.edu.cn
Department of Engineering Mechanics, Tsinghua University, Beijing 100084, China

MEI XU: xumei@tsinghua.edu.cn
Department of Engineering Mechanics, Tsinghua University, Beijing 100084, China

XUYUE WANG: wangxuyue@tsinghua.edu.cn
Department of Sciences, Harbin Institute of Technology, Shenzhen Graduate School, Shenzhen 518055, China

BIN GU: bin.gu@aeromech.usyd.edu.au
Centre for Advanced Materials Technology (CAMT), School of Aerospace, Mechanical and Mechatronic Engineering J07, The University of Sydney, NSW 2006, Australia